Northumbria Research Link

Northumbria
University
NEWCASTLE

PAPER

Sea Coral-like $NiCo_2O_4$@(Ni, Co)OOH Heterojunctions for Enhancing Overall Water-Splitting

Received 00th January 20xx,
Accepted 00th January 20xx

DOI: 10.1039/x0xx00000x

www.rsc.org/

Leiming Tao,[a] Man Li, [a] Shaohang Wu,[a] Qinglong Wang, [a] Xin Xiao,[a] Qingwei Li, [a] Mingkui Wang, [a] YongQing Fu*[b] and Yan Shen,*[a]

It is highly challenging to develop efficient and low-cost catalysts to meet stringent requirements on high current density for industrial water electrolysis application. We developed sea coral-like $NiCo_2O_4$@(Ni, Co)OOH heterojunctions, synthesized based on an epitaxial in-grown method using poly(ethylene glycol) (PEG) as a template, and explored its as efficient electrocatalyst for water-splitting. A two-electrode based alkaline electrolyzer was fabricated using $NiCo_2O_4$@(Ni, Co)OOH|| $NiCo_2O_4$@(Ni, Co)OOH, which achieved a current density value of 100 mA·cm^{-2} with a low potential of 1.83 V and high current density approached 600 mA·cm^{-2} at potential of 2.1 V along with a strong stability. These are superior to most reported data for the electrocatalysts operated at high current densities. *In-situ* calculations based on density function theory reveal that the occurrence of water-splitting on the $NiCo_2O_4$@(Ni, Co)OOH heterojunction surface. First-principles molecular dynamics simulation reveals that the stretching vibrations of metallic bonds of $NiCo_2O_4$@(Ni, Co)OOH heterojunctions open the hydrogen bonds of water. Understanding the mechanism of water-splitting at the heterojunction from *in-situ* theoretical calculations is helpful to develop new generation industrial catalysts.

Introduction

Hydrogen as one of the best sustainable energy carriers has been regard as one of the alternatives fuels to meet the future global energy demand, which are environmentally friendly and carbon free. However, it is highly challenging to develop efficient and low-cost catalysts to meet the stringent requirements on high current density (or high power density) for industrial water electrolysis applications. [1] There is a significant progress in the past a few years for developing low-cost catalysts from earth-abundant and non-noble-metal materials for hydrogen evolution reaction (HER) (e.g., boride, phosphides, chalcogenides, and titanate) [2-5] and for oxygen evolution reaction (OER) (e.g., nitrides, oxides, hydroxides, and oxyfluoride). [6-9]

Transition metal sulfides, selenides, nitrides, and phosphides have been applied as active HER catalysts. [10-13] Many reports also claimed that these materials are highly efficient OER catalysts and popularly regarded as 'bifunctional catalysts'. However, it is well-known that metal sulfides are thermodynamically less stable than metal oxides under oxidizing potentials and metal nitrides and phosphides are less stable than sulfides and so forth. [14] In fact, these oxidation processes are happening everyday in natural environments and are responsible for the transformation and formation of many minerals and rocks. Therefore, metal sulfides, selenides, nitrides, and phosphides can be oxidized easily to their corresponding metal oxides/hydroxides, especially in aqueous and strongly oxidative environments as the OER.

$NiCo_2O_4$, one of the popular cobalt-based spinel oxides, has become an emerging electrode material attributed to its easy material availability, simplified preparation, low cost, and good corrosion stability in alkaline electrolytes. [15-18] However, due to the requirement on large uphill-conversion-energy for water-splitting, it is difficult to significantly increase its electrochemical activities. [19, 20] Previous reports confirmed hierarchical $NiCo_2O_4$ hollow structures that consist of 1D nanostructures for high performance overall water-splitting and considered that nanostructures promoted the release of evolved gas bubbles and exhibited maximum catalytic performance.[21] $NiCo_2O_4$ surface modification with other materials facilitated proton transfer and dissociation and was regarded as an effective way to enhance the activity on the catalysis. [22, 23] For example, Wang *et al*. reported a novel hollow core-shell Ni@$NiCo_2O_4$ to improve the electronic conductivity of $NiCo_2O_4$ owing to the hollow Ni directly attached to the conductive Ni foam. The hollow core-shell Ni@$NiCo_2O_4$ electrode showed excellent catalytic activity with a current density of 10 mA·cm^{-2} at a bias of 1.58 V. [24] These are not enough to reveal the catalytic nature and helpful to

[a] *Wuhan National Laboratory for Optoelectronics, Huazhong University of Science and Technology, Luoyu Road 1037, Wuhan 430074, P. R. China. Y.S. (email: ciac_sheny@mail.hust.edu.cn).*
[b] *Faculty of Engineering and Environment, Northumbria University, Newcastle upon Tyne, NE18ST, UK. Y. F. (email: richard.fu@northumbria.ac.uk)*
Electronic Supplementary Information (ESI) available: [details of any supplementary information available should be included here]. See DOI: 10.1039/x0xx00000x

develop stronger catalysts. In recent years, the good optical property of semiconductor heterojunction has received extensive attention for applications in photoelectrochemical water splitting and nano materials. [25, 26] It leads to much enhanced electrocatalytic performance to develop heterojunction electrode materials, where the two structurally matching nanophases are synergized by an epitaxial in-grown interface. [27] Therefore, integrating the advantages of the HER and OER electrocatalysts to construct novel heterostructures, which possess binding affinities to both hydrogen and oxygen-containing intermediates, is extremely beneficial for enhancing the overall electrochemical water-splitting activity. For example, Yang et al. proposed to form a hydrogen bonds $O_s\cdots H\text{-}O_{ad}$ (O_s and O_{ad} denoted the surface oxygen atom of transition metal oxides and the oxygen atom of the adsorbed hydroxyl group or water molecule without bonded to transition metals, respectively) on a reconstructed nanocrystal surface to facilitate proton transfer and dissociation, leading to an enhanced water-splitting activity. [28] Previous reports have identified heterojunctions can reduce the energy barrier of water-splitting and optimize the intermediates adsorption/desorption from *ex-situ* theoretical calculations. [29, 30] However, understanding water-splitting on the heterojunction surfaces from *in-situ* theoretical calculations are pivotal for enhancing overall water-splitting, because of their outstanding chemisorptions of H_2O and intermediates.

In this paper, we designed and fabricated sea coral-like $NiCo_2O_4$@(Ni, Co)OOH heterojunctions for water-splitting. The approach includes formation of the precursors by integrating PEG into sea coral-like $NiCo_2$-PEG intermediate compounds (from Ni/Co-based nitrate with the mole ratio of Ni to Co being 1/2) and conversion of $NiCo_2O_4$@(Ni, Co)OOH heterojunctions using epitaxial in-grown method. The $NiCo_2O_4$@(Ni, Co)OOH heterojunctions exhibited high catalytic activity and excellent durability, achieving a current density of 10 mA·cm^{-2} at a low overpotential of 120 mV for HER and 220 mV for OER, respectively. A $NiCo_2O_4$@(Ni, Co)OOH||$NiCo_2O_4$@(Ni, Co)OOH two-electrode alkaline electrolyzer achieved a current density of 100 mA·cm^{-2} at a low cell bias of 1.83 V. First-principles molecular dynamics simulation reveals that the stretching vibrations of metallic bonds of the $NiCo_2O_4$@(Ni,Co)OOH heterojunctions open the hydrogen bonds of water.

Experimental Section

Preparation and characterization

Morphology, chemical compositions, and electrochemical characterization of all samples presented in the supporting information.

Computational Detail

Density function theory (DFT) calculation was performed using a plane-wave pseudopotential function, aided by the Accelrys Materials Studio (Accelrys Inc.) graphical frontend interface. The exchange correlation functional was applied using a generalized gradient approximation (GGA) with the Perdew–Burke–Ernzerh (PBE) functional. [31] The geometries of all the systems were optimized, in which a conjugated gradient technique was used in a direct minimization of the Kohn-Sham energy functional, and pseudopotentials were employed to represent the core electrons. Plane-wave functions were used as basis sets. [32]

Initial adsorption structures

As shown in Figure 1a, the XRD patterns of crystalline $NiCo_2O_4$@(Ni, Co)OOH showed that the peaks of (311) and (001) were the main strong peaks of $NiCo_2O_4$ and (Ni, Co)OOH, respectively. According to the XRD result and previous finding,[33] $NiCo_2O_4$(311), (Ni, Co)OOH(001) and $NiCo_2O_4$@(Ni, Co)OOH heterojunction (a layer (Ni, Co)OOH(001) coated onto $NiCo_2O_4$(311)) were selected for geometrical optimization. The energy cutoff was 489.8 eV and k-point mesh of 2 × 2 × 1 was used for the geometrical optimization calculations. To simulation a realistic surface catalysis reaction, our calculations were at 100% high coverage regimes on the surface with 1/4 of a monolayer of intermediates (H_2, H*, H_2O*, HO*, O*, HOO*, OO*, and O_2) and 3/4 of a monolayer of water. The coverage regime was described in previous literature. [34] The intermediates of H_2O^*, H_2^*, H^*, HO^*, O^*, HOO^*, and O_2^* were put on the top of $NiCo_2O_4$@(Ni, Co)OOH surface. The initial distances between intermediates and the corresponding active sites were set as 1.0 Å. The adsorption energy was defined as $E_b = E_{total} - E_{surf} - 3\cdot E_{H2O} - E_{inter}$ where E_{total} and E_{surf} are the total energies of the surface with and without adsorbates (including three water and one intermediate), respectively, E_{H2O} is the energy of water, and E_{inter} is the energy of intermediates (H_2, H*, H_2O*, HO*, O*, HOO*, OO*, and O_2).

First-principles molecular dynamics (FPMD) simulations

The optimized H_2O/$NiCo_2O_4$@(Ni, Co)OOH interface model was adopted for the FPMD simulations, in which the bottom layer atoms were fixed and other atoms and water molecules were allowed to relax. The energy cutoff was 489.8 eV and a k-point mesh of 2 × 2 × 1 was used for the FPMD calculations. The FPMD calculations were run for 200 steps to reach equilibrium in the NVE using eXtended-Lagrangian (XL-BOMD) molecular dynamics at a temperature of 273 K with a time step of 1 fs for motion equation integration. [35, 36]

Results and Discussion

Scheme 1 illustrates the synthesis approach and microstructure of $NiCo_2O_4$@(Ni, Co)OOH heterojunction. The chemical reaction mechanisms for $NiCo_2O_4$@(Ni, Co)OOH heterojunction can be summarized Reaction 1-7. To simplify the reaction equations, the PEG400 molecule, $HO(CH_2CH_2O)_nH$ (n = 8-9), is written as ROH and the anion, $HO(CH_2CH_2O)_n^-$, as written RO^-.

$$Ni^{2+} + 2ROH \leftrightarrow Ni(RO)_2 + 2H^+ \quad (1)$$

$$Co^{3+} + 3ROH \leftrightarrow Co(RO)_3 + 3H^+ \quad (2)$$

$$Ni(RO)_2 + 3Co(RO)_3 + 8H_2O \rightarrow (Ni, 2Co)(OH)_8 + 8ROH \quad (3)$$

$$8(Ni, 2Co)(OH)_8 \rightarrow 4NiO + 4Co_2O_3 + 4(Ni, Co)OOH + 30H_2O + 5O_2 \quad (4)$$

$$NiO + Co_2O_3 \rightarrow NiCo_2O_4 \quad (5)$$

$$NiCo_2O_4 + (Ni, Co)OOH \rightarrow NiCo_2O_4\ @(Ni, Co)OOH \quad (6)$$

$$ROH+mO_2 \rightarrow xCO_2+yH_2O \quad (7)$$

The complexation reaction of PEG400 and Ni^{2+} (or Co^{3+}) has been proposed by Faidi *et al* (Reactions 1 and 2).[37] The $NiCo_2$-PEG intermediate compounds combine with H_2O thus forming the (Ni, 2Co)$(OH)_8$, which generate NiO, Co_2O_3, and (Ni, Co)OOH during the following pyrolysis process (Reactions 3 to 4). $NiCo_2O_4$ is produced by reaction between NiO and Co_2O_3 (Reaction 5). The $NiCo_2O_4$@(Ni, Co)OOH heterojunction is formed with an epitaxial the (Ni, Co)OOH growth on $NiCo_2O_4$ (Reaction 6). Finaly, the PEG is pyrolysised into CO_2 and H_2O(Reaction 7).

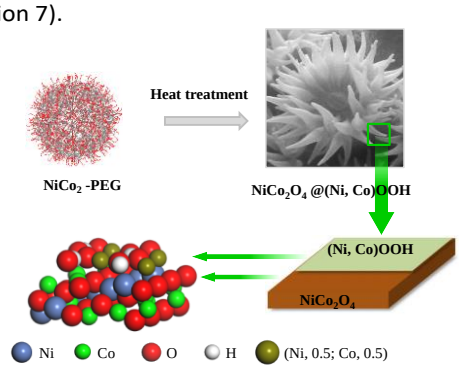

Scheme 1. Schematic illustration for synthesis and microstructures of the sea coral-like $NiCo_2O_4$@(Ni, Co)OOH heterojunction.

Figure 1a shows the XRD patterns of crystalline $NiCo_2O_4$@(Ni, Co)OOH heterojunction. The XRD peaks at 31.1°, 36.7°, 44.6°,and 59.1°correspond to (220), (311), (400), and (511) of $NiCo_2O_4$ (JCPDF # 20-0781) and at 19.1°, 38.7°, and 65°correspond to (001), (101), and (440) of (Ni, Co)OOH (JCPDF # 29-0491) components. The peaks of (311) and (001) is the main strong peaks of $NiCo_2O_4$ and (Ni, Co)OOH, respective. According to the XRD result, $NiCo_2O_4$(311), (Ni, Co)OOH(001) and $NiCo_2O_4$@(Ni, Co)OOH heterojunction (a layer (Ni, Co)OOH(001) coated onto $NiCo_2O_4$(311)) were selected for computational geometrical optimization.

The FT-IR results are shown in Figure 1b. The FT-IR results demonstrate that the $NiCo_2O_4$@(Ni, Co)OOH heterojunction contain NiO, Co_2O_3 and -OOH stretching vibration peaks. The absorption peaks around 3200−3650 cm^{-1} can be assigned to the bending and stretching vibration modes of oxygen-hydrogen groups for chemisorbed/physisorbed water molecules onto the $NiCo_2O_4$@(Ni, Co)OOH surface. [38] The peak located from 400 to 900 cm^{-1} is assigned to be the NiO and Co_2O_3 stretching vibration modes (blue). [39, 40] The absorption peaks at 1550 to 1600 cm^{-1} and 1350 to 1450 cm^{-1} are assigned to be the H_2O bending vibration mode and OOH stretching vibration mode, respectively (green). [41]

The XPS analysis results further prove the ingredients of $NiCo_2O_4$@(Ni, Co)OOH heterojunction with the same information of those from the XRD (Figure 1a) and FT-IR analysis (Figure 1b). Figure 1c shows the high-resolution XPS spectrum of O1s, which can be deconvoluted into three peaks. The first peak at 529.39 eV is assigned to the metal oxides, which are related to NiO and Co_2O_3. The peak at 531.5 eV can be assigned to the oxygen in the hydroxide group (OH^-), which are linked with surface phases of γ-NiOOH and γ-CoOOH. [42] The peaks at 533.5 can be assigned to the surface adsorption of H_2O [43]. The XPS spectrum of Co in the $NiCo_2O_4$@(Ni, Co)OOH can be deconvoluted into four peaks (Figure 1d). For this study, the spin orbit level energy spacing is around 15eV (Figure 1d), so the characteristic peaks is Co^{3+} of Co_2O_3. [43] Whereas the Co $2p_{1/2}$ in the $NiCo_2O_4$@(Ni, Co)OOH only shows a major peak at 795.6 eV, which is ascribed to CoOOH. The peaks of 854.4 and 872.1 eV are attributed to NiO (Figure 1e). Whereas the peaks at 856.0 and 873.6 eV are corresponding to NiOOH (Figure 1e).

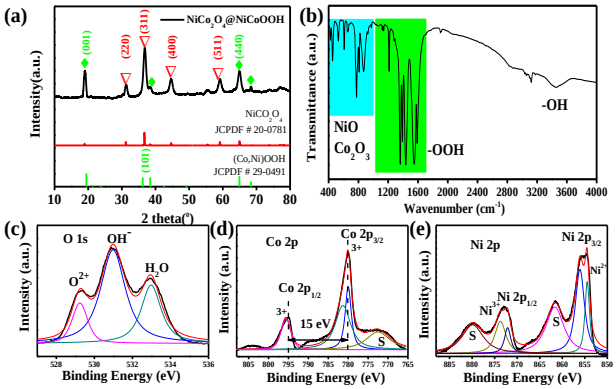

Figure 1. Results of the $NiCo_2O_4$@(Ni, Co)OOH heterojunction for a) X-ray diffraction (XRD) patterns; b) FT-IR transmission spectrum in region 400-4000 cm^{-1}, (1) and (2) with enlargement region 400-1000 cm^{-1} (blue) and 1000-1750 cm^{-1} (green); c)-e) High-resolution XPS spectra of O 1s, Co 2p, and Ni 2p, where 'S' represents non-stoichiometry peak.

Morphology and structure of the as obtained Ni–Co based precursor was characterized using the FE-SEM, and the results are shown in Figure S1. It shows that the precursors are hollow micro-cone structure with an average length of approximately 10 μm (Figure S1a). The magnified SEM images (Figures S1b) further reveals that these hollow microcuboids constitute 2D nanosheets. The FE-SEM image of the $NiCo_2O_4$@(Ni, Co)OOH sample shows the hollow micro-cone morphology(Figure 2a), which looks like sea corals (Figure 2b). The sea coral-like $NiCo_2O_4$@(Ni, Co)OOH consists of the stamen with length of approximately 1.5 μm and petals with tiny hair-like structure (Figure 2b). The corresponding EDX mapping reveals uniform distributions of O, Co and Ni elements (Figure 2c). These petal structures are consisted of low-dimensional building blocks of ultrathin nanosheets according to the TEM image (Figure 2d). The ultrathin nanosheets (green frame area in Figure 2d) were further characterized using the SAED (Figure 2d inset) and an HRTEM image (Figure 2e). For the yellow arrowhead region (Figure 2e), TEM image reveals that the $NiCo_2O_4$@(Ni, Co)OOH crystals are surrounded by the interlinked channels with an average width of 5 nm, which could behave as the capillary channels of ion and gas transport. The Figure 2e blue frame area is magnified to Figure 2f. As Figure 2f shown, the heterostructure of $NiCo_2O_4$@(Ni, Co)OOH can be observed. The lattice parameter at the red arrowhead was measured to be 0.45 nm, corresponding to the (100) crystal plane of the (Ni,

Co)OOH (Figure 2f). The lattice parameter at the black arrowhead was measured to be 0.24 nm, corresponding to the (311) crystal plane of $NiCo_2O_4$ (Figure 2f). The HRTEM results are in good agreements with the XRD analysis (Figure 1a) and SAED pattern (Figure 2d inset). In brief, SEM and (HR)TEM analysis show that the hierarchical structures of the $NiCo_2O_4$@(Ni, Co)OOH heterojunction are consisted of capillary (mesoporous, with width of 5 nm) channels, petals with medium pore diameter (macroporous, with width of 100 nm) channels, and the stamen with large (microns) channels. These results can well-explain that the BET measurement results of a wide pore size distribution and large surface areas (Figure S2).

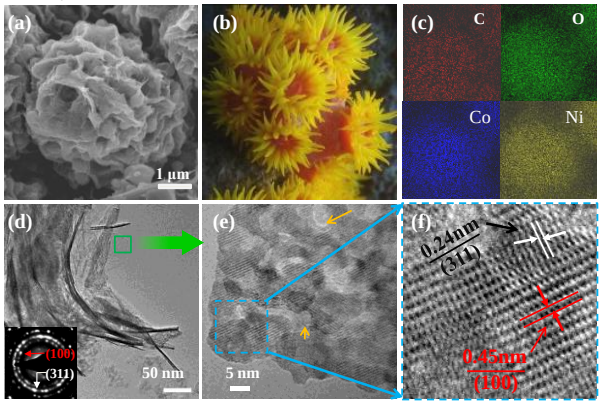

Figure 2. Results of $NiCo_2O_4$@(Ni, Co)OOH heterojunction for a) the field emission scanning electron microscopy (FE-SEM) b) a photograph of sea coral, c) the corresponding EDX mapping images of C, O, Co and Ni elements, d) the transmisssion electron microscopy (TEM) with SAED pattern (inset), e) and f) the high resolution transmisssion electron microscopy (HR-TEM).

The activities of nanostructured catalysts could be partially enhanced due to their increased electrochemical surface areas (see Supporting Information for details of the electrochemical surface area (ECSA)). [44] We have corrected the electrochemical measurements by removing the contribution of ECSA. Figures 3a and 3b present the HER and OER polarization curves for the $NiCo_2O_4$@(Ni, Co)OOH heterojunction in 1.0 M KOH solution at a scan rate of 5 $mV{\cdot}s^{-1}$. The $NiCo_2O_4$@(Ni, Co)OOH heterojunction has an potential of −120 mV at a current density of 10 $mA{\cdot}cm^{-2}$ (Figure 3a), which is lower than that of the Pt/C (−60 mV), but is higher than that of $NiCo_2O_4$ (−180 mV). Figure 3b presents the OER polarization curves with a current density of 10 $mA{\cdot}cm^{-2}$, and the overpotential values follows the order from low to high with a sequence of: RuO_2 (200 mV) <$NiCo_2O_4$@(Ni, Co)OOH(220 mV) <$NiCo_2O_4$(240 mV), whereas the previously reported $NiCo_2O_4$@NiO@Ni with a larger OER overpotential (280 mV). [45] The $NiCo_2O_4$@(Ni, Co)OOH heterojunction exhibits a better electrocatalytic activity than the data of the $NiCo_2O_4$. Table S1 shows the comparison of HER and OER activity for $NiCo_2O_4$@(Ni, Co)OOH heterojunction with other recently published highly active electrocatalysts in alkaline electrolyte (1 M KOH). Clearly, $NiCo_2O_4$@(Ni, Co)OOH heterojunction exhibits excellent property of HER and OER in alkaline electrolyte.

The catalytic kinetics of $NiCo_2O_4$@(Ni, Co)OOH heterojunction assessed by the Tafel plots are shown in Figures 3c and 3d, which were derived from the Koutecky-Levich plots (Figure S3). The Tafel slopes provide the detailed information of reaction mechanism and catalytic activity. A smaller Tafel slope indicates that the overpotential of the catalytic reaction is lower at the same dynamic current density or apparent current density.[46] As shown in Figure 3c, the obtained Tafel slope of the $NiCo_2O_4$@(Ni, Co)OOH (60 $mV{\cdot}dec^{-1}$) is lower than that of $NiCo_2O_4$ (63 $mV{\cdot}dec^{-1}$). The results show that the $NiCo_2O_4$@(Ni, Co)OOH heterojunction has a superior HER reaction kinetics (Figure 3c). The result of Tafel plot for OER reaction kinetics shows that the $NiCo_2O_4$@(Ni, Co)OOH (48 $mV{\cdot}dec^{-1}$) has a slope value which is lower than that of $NiCo_2O_4$ (53 $mV{\cdot}dec^{-1}$), indicating that the $NiCo_2O_4$@(Ni, Co)OOH has a faster OER reaction kinetics than $NiCo_2O_4$. We further analysed the catalytic dynamics in terms of turn-over frequency (TOF) of $NiCo_2O_4$@(Ni, Co)OOH and $NiCo_2O_4$ towards the HER and OER. The TOF (0.22 s^{-1}) of the $NiCo_2O_4$@(Ni, Co)OOH heterojunction is higher than that of $NiCo_2O_4$ (0.15 s^{-1}) which were obtained at an overpotential of 0.20 V for HER (Figure 3c inset). TOF (0.2 s^{-1}) of the $NiCo_2O_4$@(Ni, Co)OOH heterojunction is also higher than that of $NiCo_2O_4$ (0.12 s^{-1}) for OER under an overpotential of 0.20 V (Figure 3d inset). Here, we further studied the Faradic efficiency of the OER for various electrodes using the RRDE technique. When a constant current (300 μA) was applied to the disk electrode for O_2 generation, a ring current of about 59.7 μA and 58 μA could be detected on the ring electrodes with $NiCo_2O_4$@(Ni, Co)OOH and $NiCo_2O_4$ catalysts (Figure S4a and S4b). Therefore, the Faradaic efficiency of $NiCo_2O_4$@(Ni, Co)OOH and $NiCo_2O_4$ was determined to be 99.5% and ~96.7%, suggesting that the former has higher catalytic activity towards OER.

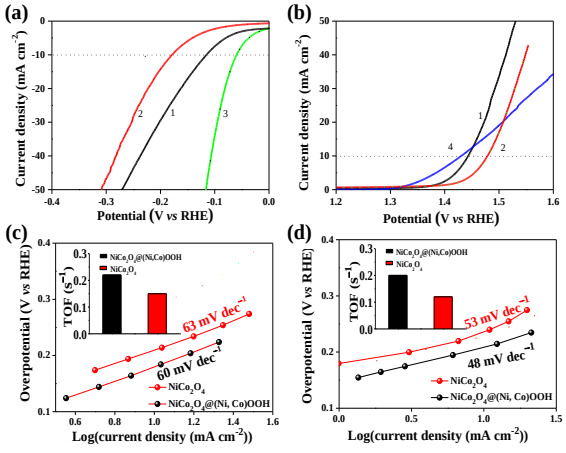

Figure 3. Electrochemical measurements: linear sweep polarization curves (LSV) of $NiCo_2O_4$@(Ni, Co)OOH (curve 1), $NiCo_2O_4$ (curve 2), Pt/C (curve 3), RuO_2 (curve 4) for a) HER and b) OER; the corresponding Tafel slopes of $NiCo_2O_4$@(Ni, Co)OOH (black) and $NiCo_2O_4$ (red) for c) HER and d) OER; The turnover frequency (TOF) of specific activity and mass activity at overpotential of 200 mV for in 1 M KOH (inset).

We then further demonstrated high-performance two-electrode water electrolysis cells ($NiCo_2O_4$@(Ni, Co)OOH||$NiCo_2O_4$@(Ni, Co)OOH) for overall water splitting. The $NiCo_2O_4$@(Ni, Co)OOH heterojunction merely required bias voltages of 1.61, 1.66, and 1.83 V to reach current densities of 10, 20, and 100 mA·cm^{-2} (Figure 4a). This is superior to previously reported electrocatalysts (Table S2), for examples, $NiCo_2O_4$ hollow microcuboids (1.74 V at 20 mA·cm^{-2}) [21], NiFe/$NiCo_2O_4$/NF (1.67 V at 20 mA·cm^{-2}) [47], and $NiCo_2O_4$ nanosheet array (1.74 V at 20 mA·cm^{-2}) [48]. Our fabricated $NiCo_2O_4$@(Ni, Co)OOH exhibited an excellent stability for 28 hours of water electrolysis without obvious degradation during a test at a constant potential of 1.83 V (Figure 4a inset). Furthermore, The $NiCo_2O_4$@(Ni, Co)OOH || $NiCo_2O_4$@(Ni, Co)OOH exhibited the stability for 30h with the current density increased from 0.1 to 0.6 A·cm^{-2} in the two-electrode device (Figure 4b) and the XRD and HRTEM of $NiCo_2O_4$@(Ni, Co)OOH heterojunction was shown after 30h water-splitting in Figure S5. The results showed that high current density approached 0.6 A·cm^{-2} (6,000 A·m^{-2}) at potential of 2.1 V with a good stability for 10 hours. The photograph of water electrolysis in the inset in Figure 4b exhibited gas evolution on both electrodes at a current density of 100 mA·cm^{-2}. It was shown in the supporting information Movie S1. The gas chromatography survey clearly confirms that the produced bubbles are H_2 and O_2 (Figure S6a). The Faradaic efficiency (FE) of experimental H_2 (black square) and O_2 (red sphere) production were versus the theoretic 98% quantities (solid line) for overall water splitting of $NiCo_2O_4$@(Ni, Co)OOH in 1 M KOH at 100 mA·cm^{-2} (Figure S6b). The concentrations of Co and Ni were detected by inductively coupled plasma mass spectrometry (ICP-MS). The levels of Co and Ni in the solution after durability test were 0.5 and 0.3 μg·L^{-1}, respectively. The level is lower than 50 μg·L^{-1} of the environmental protection standard (Discharge Standard of Water Pollutants for Industry (GB8978-1996)). It is important to confirm the environmental safety of the process. Our newly designed catalyst can satisfy the stringent requirements of high current density in the industrial water electrolysis applications.

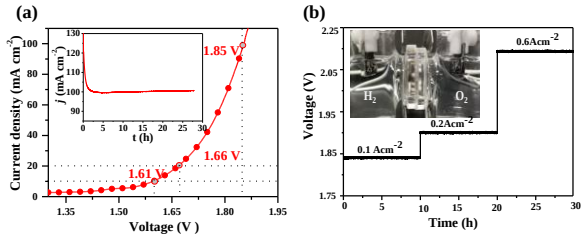

Figure 4. a) Electrolyzer properties of $NiCo_2O_4$@(Ni, Co)OOH || $NiCo_2O_4$@(Ni, Co)OOH (the dot horizontal line is a guide to show a current density of 10, 20, and 100 mA·cm^{-2}) and the chronoampermetric curves for long-term water electrolysis at a static potential of 1.83V (inset). b) Multi-current steps of $NiCo_2O_4$@(Ni, Co)OOH||$NiCo_2O_4$@(Ni, Co)OOH for long-term with the current density increased from 0.1 to 0.6 A·cm^{-2} in the two-electrode device. The inset is an optical photograph of $NiCo_2O_4$@(Ni, Co)OOH||$NiCo_2O_4$@(Ni, Co)OOH for the generation of H_2 and O_2 at a current density of 100 mA·cm^{-2}.

The lower overpotential and Tafel slope of $NiCo_2O_4$@(Ni, Co)OOH than that of $NiCo_2O_4$ suggest that the $NiCo_2O_4$@(Ni, Co)OOH heterojunction can lower down the activation energy of water-splitting and also enhance the activity of the catalysis processes. In order to understand this effect on the enhanced overall water-splitting performance of $NiCo_2O_4$@(Ni, Co)OOH heterojunction, we performed density function theory (DFT) calculations to investigate the binding energies of the intermediates (H_2O*, HO*, O*, HOO*, OO*, H*, H_2*, and O_2* species) and product (O_2 and H_2) on the $NiCo_2O_4$ and the $NiCo_2O_4$@(Ni, Co)OOH surfaces, respective.

Figure 5a shows the models for $NiCo_2O_4$ and $NiCo_2O_4$@(Ni, Co)OOH heterojunction surface and water-splitting reaction on $NiCo_2O_4$@(Ni, Co)OOH heterojunction surfaces in an alkaline electrolyte. The four electron reaction paths (Figure 5a) (①-④) are shown:[49]

Cathode: $2H_2O + 2e^- \rightarrow 2OH^- + H_2$ (8)

Anode: $4OH^- \rightarrow HO^* + 3OH^- + e^-$ (9)

$\rightarrow O^* + H_2O + OH^- + 2e^-$ (10)

$\rightarrow HOO^* + H_2O + OH^- + 3e^-$ (11)

$\rightarrow O_2 + 2H_2O + 4e^-$ (12)

We calculated the energy for Reactions 8-12 and its change (ΔE).[50] The catalytic performance can be estimated by the magnitude of potential, which determines the rate-limiting step toward the HER and OER, i.e. ΔE_{HO*} ($\Delta E_{HO*} = E(HO*) - E(*) - (E_{H2O} - 1/2E_{H_2})$). Therefore, the slowest step, i.e., the specific reaction in the four-step mechanism, should exhibit the largestΔE_{OER}: ΔE_{OER}= Max [ΔE_1 , ΔE_2 , ΔE_3 , ΔE_4] (Figure 5a). Figure 5b shows the corresponding binding energies of H_2, H_2*, H*, H_2O*, HO*, O*, HOO*, O_2*, and O_2 on the $NiCo_2O_4$@(Ni, Co)OOH heterojunction surface (black histogram) and $NiCo_2O_4$ surface (red histogram), and their-difference (greenbox). These are two normal distribution for red histogram and black histogram, where the distribution rangs from ΔE_{H2} to ΔE_{H2O*} and ΔE_{H2O*} to ΔE_{O2}, respective. While, the trend of their binding energies difference (green box) is two sanddle-shapped distribution from ΔE_{H2} to ΔE_{O2}. The detials are summarized in Table 1. For the cathodic reaction (i.e., the HER), the binding energy values of the H* (ΔE_{H*}) on $NiCo_2O_4$@(Ni, Co)OOH heterojunction and $NiCo_2O_4$ surface are 1.08 and 2.74 eV, and the binding energy difference is −1.68 eV. The value of ΔE_{H*} on the two catalysts is the maximum among those ofΔE_{H2}, ΔE_{H2*}, and ΔE_{H2O*} (Table 1). Accordingly, we conclude the adsorption of H* is the potential-determining step during the HER process. For the cathodic reaction, the ΔE_{O*} is the maximum among those of ΔE_{H2O*} , ΔE_{HO*} , ΔE_{HOO*} , ΔE_{O2*} , and ΔE_{O2} on the $NiCo_2O_4$@(Ni, Co)OOH heterojunction and $NiCo_2O_4$ surface, respective. The ΔE_{O*} on the $NiCo_2O_4$@(Ni, Co)OOH heterojunction and $NiCo_2O_4$ surface are 1.74 and 4.42 eV, and their binding energy difference is −3.48 eV. Therefore，the O*

adsorption is the potential-determining step for the OER. The ΔE_{O*} is bigger than ΔE_{H*}, indicating electron reaction path ③ is the slowest step (Figure 5a). The calculation results clearly show that the $NiCo_2O_4$@(Ni, Co)OOH heterojunction surface has lower binding energy for the HER and OER if compared with the $NiCo_2O_4$ surface (Figure 5b). A low binding energy facilitates the dissociation of H_2O molecules and eventually release of H_2 and O_2. For example, the difference in binding energy of H_2 on the $NiCo_2O_4$@(Ni, Co)OOH heterojunction surface and $NiCo_2O_4$ surface is 1.14 eV, meaning the $NiCo_2O_4$@(Ni, Co)OOH heterojunction can facilitate the release of H_2 compared with $NiCo_2O_4$. The difference in binding energy of H* is −1.68 eV, meaning the $NiCo_2O_4$@(Ni, Co)OOH heterojunction needs a less energy compared with $NiCo_2O_4$. Our DFT calculations demonstrate that the activation energy of water-splitting can be lowered by $NiCo_2O_4$@(Ni, Co)OOH heterojunction than that of $NiCo_2O_4$.

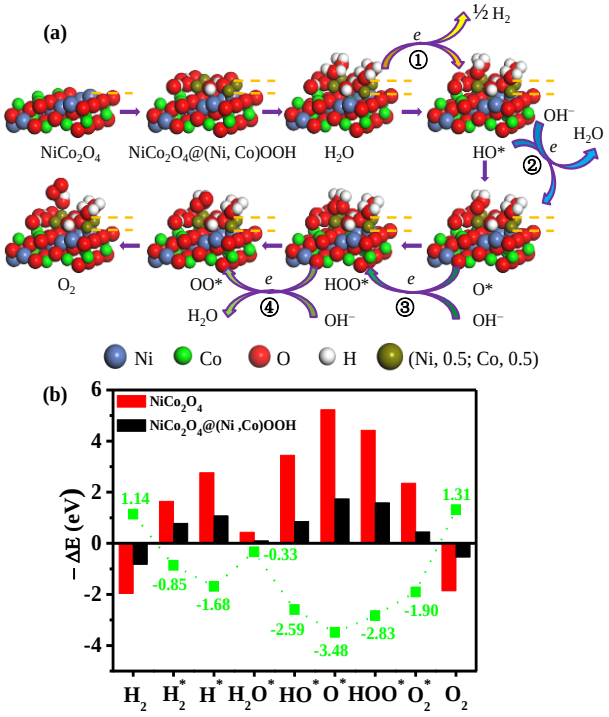

Figure 5. a) Water splitting reactions on the $NiCo_2O_4$@(Ni, Co)OOH heterojunction surface in an alkaline electrolyte. b) The energy-difference (green) of the corresponding binding energies of H_2^*, H^*, H_2O^*, HO^*, O^*, HOO^* and O_2^* dissociation on $NiCo_2O_4$-(311) surface (red) and $NiCo_2O_4$@(Ni, Co)OOH surface (black).

First-principles molecular dynamics (FPMD) simulations provides a dynamic model to monitor the water-splitting on the surfaces of $NiCo_2O_4$, (Ni, Co)OOH, and $NiCo_2O_4$@(Ni, Co)OOH heterojunction, respectively. Figures 6a-6c and 6d-6f show the initial and final structures of water on the surfaces of $NiCo_2O_4$, (Ni, Co)OOH, and $NiCo_2O_4$@(Ni, Co)OOH heterojunction before and after the molecular dynamics simulations (the detailed simulation animations of movies are shown in Movie S2). From the analysis results of $NiCo_2O_4$@(Ni, Co)OOH heterojunction, the stretch vibrations of the metallic bond (one metal atom is bonded to another secondary metal atom) open the hydrogen bond of the water (Movie S2). For the $NiCo_2O_4$, the simulation results show a similar decomposition mechanism of water as that of the $NiCo_2O_4$@(Ni, Co)OOH heterojunction. Whereas for the (Ni, Co)OOH, there needs a hydrogen bond stretches of O_s···H-O_{ad} in order to break the bonds of water. [28] There are weak vibrations of the atoms from the second layer and below for the $NiCo_2O_4$ (Movie S2), if compared with that of the (Ni, Co)OOH). Compared to the $NiCo_2O_4$, a monolayer of (Ni, Co)OOH on the $NiCo_2O_4$ surface can enhance the activity based on above results of the binding energy. The FPMD results show the water-splitting mechanisms for different materials. For the $NiCo_2O_4$@(Ni, Co)OOH heterojunction and $NiCo_2O_4$, it is the stretching vibrations of the metallic bonds to open the hydrogen bonding of water; whereas for the (Ni, Co)OOH, it is the stretching vibrations of short hydrogen bonds of O_s···H-O_{ad} to open the hydrogen bonding of water.

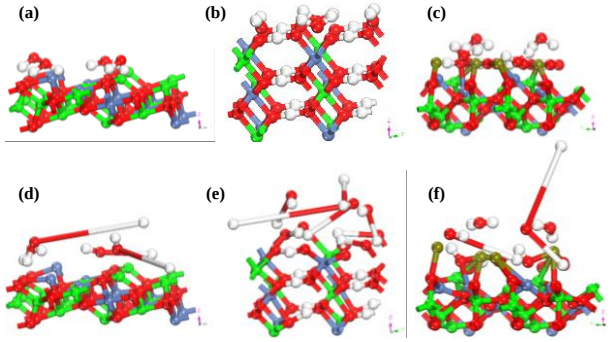

Figure 6. The Initial structures of a)-c) and final structuresof d)-f) taken from the first principle molecular dynamics (FPMD) simulations of water on $NiCo_2O_4$, (Ni, Co)OOH, and $NiCo_2O_4$@(Ni, Co)OOH heterojunction at 273K, respectively.

The DFT calculation shown above already demonstrated that adsorption energy of the $NiCo_2O_4$@(Ni, Co)OOH heterojunction with the corresponding intermediates is much lower than that of the $NiCo_2O_4$ surface, thus facilitating the dissociation of the H_2O molecule and the release of H_2 and O_2. *In-situ* calculations based on density function theory reveal that the occurrence of water-splitting on the $NiCo_2O_4$@(Ni, Co)OOH heterojunction surface. First-principles molecular dynamics simulation reveals that the stretching vibrations of the metallic bonds in the $NiCo_2O_4$@(Ni, Co)OOH heterojunction have opened the hydrogen bonding of water. Hence, we believe that the coral-like $NiCo_2O_4$@(Ni, Co)OOH heterojunction is promising for the industrial applications in future.

Table 1. Binging energies of H_2, H-H*, H*, H_2O*, HO*, O*, HOO*, O-O*, and O_2 (ΔE in eV) on the $NiCo_2O_4$-(311) surfaceand $NiCo_2O_4$@(Ni, Co)OOH heterojunction surfaces, and their energy-differences

	ΔE_{H2}	ΔE_{H-H*}	ΔE_{H*}	ΔE_{H2O*}	ΔE_{HO*}	ΔE_{O*}	ΔE_{HOO*}	ΔE_{O-O*}	ΔE_{O2}
$NiCo_2O_4$	-1.96	1.64	2.76	0.43	3.44	5.22	4.42	2.35	-1.86
$NiCo_2O_4$@(Ni, Co)OOH	-0.82	0.78	1.08	0.09	0.85	1.74	1.58	0.44	-0.54
Energy-difference	1.14	-0.86	-1.68	-0.33	-2.59	-3.48	-2.8	-1.90	1.31

Conclusion

In summary, the sea coral-like $NiCo_2O_4$@(Ni, Co)OOH heterojunction exhibited high catalytic activity and excellent durability, achieving a current density of 10 $mA{\cdot}cm^{-2}$ at a low overpotential of 120 mV for HER and 220 mV for OER, respectively. A $NiCo_2O_4$@(Ni, Co)OOH || $NiCo_2O_4$@(Ni, Co)OOH two-electrode alkaline electrolyzer achieved a value of 100 $mA{\cdot}cm^{-2}$ at a low cell bias of 1.83 V, Furthermore, the high current density approached 0.6 $A{\cdot}cm^{-2}$ at 2.1 V along with 10 h stability. DFT calculations demonstrate that the activation energy of water-splitting can be lowered by forming the $NiCo_2O_4$@(Ni, Co)OOH heterojunctions than that of $NiCo_2O_4$. The FPMD results revealed the different water-splitting mechanisms: e.g., for $NiCo_2O_4$@(Ni, Co)OOH heterojunction and $NiCo_2O_4$, it was the stretching vibrations of the metallic bonds to open the hydrogen bonding of water; whereas for the (Ni, Co)OOH, it was the stretching vibrations of shorter hydrogen bonds of $O_s{\cdots}H\text{-}O_{ad}$ to open the hydrogen bonding of water. We believe that $NiCo_2O_4$@(Ni, Co)OOH heterojunctions meet the stringent requirements of high current density from industrial water electrolysis applications.

Conflicts of interest

There are no conflicts to declare.

Acknowledgements

The authors gratefully acknowledge financial support from the 973 Program of China (2014CB643506), the National Natural Science Foundation of China (NSFC), the Major International (regional) Joint Research Project NSFC-SNSF (51661135023), NSFC (21673091), the Fundamental Research Funds for the Central Universities(HUST: 2016YXMS031), the Director Fund of the WNLO, the Open Funds of the State Key Laboratory of Electroanalytical Chemistry (SKLEAC201607). The authors also gratefully acknowledge UK Engineering and Physical Sciences Research Council (EPSRC) EP/P018998/1, a Newton Mobility Grant (IE161019) from the Royal Society UK and the NSFC, and Royal Academy of Engineering UK-Research Exchange with China and India. The authors thank the Analytical and Testing Center of HUST and the Center of Micro-Fabrication and Characterization of WNLO for the measurements. We thank Hu Lei for providing the calculations by Materials Studio. We thank Ren Jie for designing the drawings.

Notes and references

1. W. Li, X. F. Gao, D. H. Xiong, F. Wei, W. G. Song, J. Y. Xu and L. F. Liu, *Adv. Energy Mater.*, 2017, **7**, 1602579-n/a.
2. Y. Zhang, Y. Wang, C. Han, S. Jia, S. Zhou and J. Zang, *Nanoscale*, 2017, DOI: 10.1039/c7nr08092a.
3. M. Zhang, S. Ci, H. Li, P. Cai, H. Xu and Z. Wen, *Int. J. Hydrogen Energy*, 2017, **42**, 29080-29090.
4. H. Liu, Q. He, H. Jiang, Y. Lin, Y. Zhang, M. Habib, S. Chen and L. Song, *ACS Nano*, 2017, **11**, 11574-11583.
5. C. Dong, X. Liu, X. Wang, X. Yuan, Z. Xu, W. Dong, M. S. Riaz, G. Li and F. Huang, *J. Mater. Chem. A*, 2017, **5**, 24767-24774.
6. J. Zheng, X. Chen, X. Zhong, S. Li, T. Liu, G. Zhuang, X. Li, S. Deng, D. Mei and J.-G. Wang, *Adv. Funct. Mater.*, 2017, DOI: 10.1002/adfm.201704169, 1704169.
7. A. Kumar and S. Bhattacharyya, *ACS Appl. Mat. Interfaces*, 2017, **9**, 41906-41915.
8. K. Chakrapani, F. Özcan, K. F. Ortega, T. Machowski and M. Behrens, *ChemElectroChem*, 2017, DOI: 10.1002/celc.201700936, n/a-n/a.
9. K. Liang, L. Guo, K. Marcus, S. Zhang, Z. Yang, D. E. Perea, L. Zhou, Y. Du and Y. Yang, *ACS Catal.*, 2017, **7**, 8406-8412.
10. M. S. Faber, M. A. Lukowski, Q. Ding, N. S. Kaiser and S. Jin, *J. Phys. Chem. C*, 2014, **118**, 21347-21356.
11. B. Liu, Y.-F. Zhao, H.-Q. Peng, Z.-Y. Zhang, C.-K. Sit, M.-F. Yuen, T.-R. Zhang, C.-S. Lee and W.-J. Zhang, *Adv. Mater.*, 2017, **29**, 1606521-n/a.
12. C. Z. Zhu, S. F. Fu, J. H. Song, Q. R. Shi, D. Su, M. H. Engelhard, X. L. Li, D. D. Xiao, D. S. Li, L. Estevez, D. Du and Y. H. Lin, *Small*, 2017, **13**.
13. R. Zhang, X. Wang, S. Yu, T. Wen, X. Zhu, F. Yang, X. Sun, X. Wang and W. Hu, *Adv. Mater.*, 2017, **29**, 1605502.
14. S. Jin, *ACS Energy Lett.*, 2017, **2**, 1937-1938.
15. S. X. Liu, L. F. Hu, X. J. Xu, A. A. Al-Ghamdi and X. S. Fang, *Small*, 2015, **11**, 4267-4283.
16. J. Yang, C. Yu, S. X. Liang, S. F. Li, H. W. Huang, X. T. Han, C. T. Zhao, X. D. Song, C. Hao, P. M. Ajayan and J. S. Qiu, *Chem. Mater.*, 2016, **28**, 5855-5863.
17. S. Velraj, 2017.
18. L. Fang, Z. Jiang, H. Xu, L. Liu, Y. guan, X. Gu and Y. Wang, *J. Catal.*, 2018, **357**, 238-246.
19. B. Wang, Y. Cao, Y. Chen, R. Wang, X. Wang, X. Lai, C. Xiao, J. Tu and S. Ding, *Inorganic Chemistry Frontiers*, 2017, DOI: 10.1039/c7qi00583k.
20. Z. Wang, S. Zeng, W. Liu, X. Wang, Q. Li, Z. Zhao and F. Geng, *ACS Appl. Mat. Interfaces*, 2017, **9**, 1488-1495.
21. X. Gao, H. Zhang, Q. Li, X. Yu, Z. Hong, X. Zhang, C. Liang and Z. Lin, *Angew. Chem. Int. Ed.*, 2016, **55**, 6290-6294.
22. Y. Li, M. Afzaal and P. O'Brien, *J. Mater. Chem.*, 2006, **16**, 2175-2180.
23. L. Wang, C. Gu, X. Ge, J. Zhang, H. Zhu, and J. Tu, *Adv.*

Mater. Inter., 2017, **4**, 1700481.
24. L. Wang, C. Gu, X. Ge, J. Zhang, H. Zhu, and J. Tu, *ChemNanoMat*, 2018, **4**, 124-131.
25. J. Su, L. Guo, N. Bao and C. A. Grimes, *Nano Lett.*, 2011, **11**, 1928-1933.
26. M. T. Mayer, Y. Lin, G. Yuan and D. Wang, *Acc. Chem. Res.*, 2013, **46**, 1558-1566.
27. J. Hou, Y. Wu, S. Cao, F. Liang, Z. Lin, Z. Gao and L. Sun, *Adv. Energy Mater.*, 2017, **7**, 1700171.
28. J. Yang, J. Zheng, M. Xu, Z. Zhuo, W. Yang, L.-W. Wang, L. Dai, J. Lu, K. Amine and F. Pan, *ACS Catal.*, 2017, **8**, 466-473.
29. Q. Sun, C. Sun, A. Du, S. Dou and Z. Li, *Nanoscale*, 2016, **8**, 14084-14091.
30. J. Liu, J. Wang, B. Zhang, Y. Ruan, H. Wan, X. Ji, K. Xu, D. Zha, L. Miao and J. Jiang, *J. Mater. Chem. A*, 2018, **6**, 2067-2072.
31. B. K. Perdew John P., Wang Yue, *Phys. Rev. B: Condens. Matter*, 1996, **54**, 16533-16539.
32. P. J. D. Monkhorst Hendrik J., *Phys. Rev. B: Condens. Matter*, 1976, **13**, 5188--5192.
33. L. Tao, Y. Li, M. Li, G. Gao, X. Xiao, M. Wang, X. Jiang, X. Lv, Q. Li, S. Zhang, Z. Zhao, C. Zhao and Y. Shen, *J. Phys. Chem. C*, 2017, **121**, 25888-25897.
34. F. P. Cometto, P. Paredes-Olivera, V. A. Macagno and E. M. Patrito, *J. Phys. Chem. B*, 2005, **109**, 21737-21748.
35. A. M. N. Niklasson, P. Steneteg, A. Odell, N. Bock, M. Challacombe, C. J. Tymczak, E. Holmström, G. Zheng and V. Weber, *J. Chem. Phys.*, 2009, **130**, 214109.
36. A. M. N. Niklasson, P. Steneteg and N. Bock, *J. Chem. Phys.*, 2011, **135**, 164111.
37. S. E. Faidi, G. Jones and J. D. Scantlebury, *Electrochim. Acta*, 1987, **32**, 947-953.
38. G. Nagaraju, G. S. R. Raju, Y. H. Ko and J. S. Yu, *Nanoscale*, 2016, **8**, 812-825.
39. Z.-A. Hu, Y.-L. Xie, Y.-X. Wang, H.-Y. Wu, Y.-Y. Yang and Z.-Y. Zhang, *Electrochim. Acta*, 2009, **54**, 2737-2741.
40. F. Zhang, C. Z. Yuan, X. J. Lu, L. J. Zhang, Q. Che and X. G. Zhang, *J. Power Sources*, 2012, **203**, 250-256.
41. J.-S. Lee and S.-C. Choi, *Mater. Lett.*, 2004, **58**, 390-393.
42. B. P. Payne, M. C. Biesinger and N. S. McIntyre, *J. Electron. Spectrosc. Relat. Phenom.*, 2012, **185**, 159-166.
43. P. W. Menezes, A. Indra, D. Gonzalez-Flores, N. R. Sahraie, I. Zaharieva, M. Schwarze, P. Strasser, H. Dau and M. Driess, *ACS Catal.*, 2015, **5**, 2017-2027.
44. S. Gao, Y. Lin, X. C. Jiao, Y. F. Sun, Q. Q. Luo, W. H. Zhang, D. Q. Li, J. L. Yang and Y. Xie, *Nature*, 2016, **529**, 68-+.
45. L. Y. Wang, C. D. Gu, X. Ge, J. L. Zhang, H. Y. Zhu and J. P. Tu, *Part. Part. Syst. Char.*, 2017, **34**, 1700228.
46. J. H. Wang, W. Cui, Q. Liu, Z. C. Xing, A. M. Asiri and X. P. Sun, *Adv. Mater.*, 2016, **28**, 215-230.
47. C. Xiao, Y. Li, X. Lu and C. Zhao, *Adv. Funct. Mater.*, 2016, **26**, 3515-3523.
48. L. Fang, Z. Jiang, H. Xu, L. Liu, Y. guan, X. Gu and Y. Wang, *J. Catal.*, 2018, **357**, 238-246.
49. J. Rossmeisl, A. Logadottir and J. K. Norskov, *Chem. Phys.*, 2005, **319**, 178-184.
50. I. C. Man, H. Y. Su, F. Calle-Vallejo, H. A. Hansen, J. I. Martinez, N. G. Inoglu, J. Kitchin, T. F. Jaramillo, J. K. Norskov and J. Rossmeisl, *Chemcatchem*, 2011, **3**, 1159-1165.

PAPER

TOC

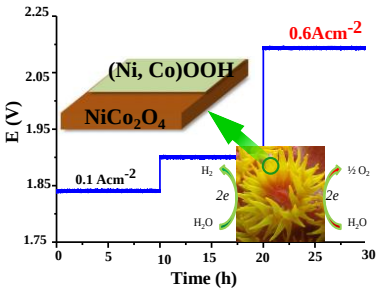

The efficient and low-cost sea coral-like $NiCo_2O_4$@(Ni, Co)OOH heterojunctions catalysts meet the high current density for industrial water electrolysis applications.

Supporting Information

Sea Coral-like $NiCo_2O_4$@(Ni, Co)OOH Heterojunctions for Enhancing Overall Water-Splitting

Leiming Tao[1], Man Li[1], Shaohang Wu[1], Qinglong Wang[1], Xin Xiao[1], Qingwei Li[1], Mingkui Wang[1], YongQing Fu[2,] *, and Yan Shen[1,] *

Supplementary Experimental Section

Characterization Measurements

Morphology, chemical compositions, and crystalline structures of all the samples were characterized using various methods. X-ray diffraction (XRD) measurements were performed using an X'pert PRO diffractometer (PANalytical B.V.) with a Cu Ka X-ray source, operated at 40 kV and 40 mA. Surface and internal microstructures were investigated using a field emission scanning electron microscope (FE-SEM, Nova NanoSEM 450) and a high resolution transmission electron microscope (HRTEM, 300 kV Titan Probe corrected TEM, Titan G2 60-300). Surface chemical states of the samples were analyzed using an X-ray photoelectron spectroscope (XPS, Thermofisher-ESCALab 250). Brunauer-Emmett-Teller (BET) surface areas (S_{BET}) and pore size distributions of samples were determined using a Micromeritics ASAP 2000 Nitrogen Adsorption apparatus. All the samples were degassed at 180 °C prior to the BET measurements. The determination of Co and Ni was carried out on an ELAN DRC-e ICP-MS(PerkinElmer Instruments Co. Ltd., USA)

Electrochemical Measurements

The catalytic activity of the prepared $NiCo_2O_4$@(Ni, Co)OOH loaded onto glassy carbon electrodes towards oxygen evolution and hydrogen evolution reactions was studied by voltammetry in a three-electrode electrochemical cell. For comparison purposes, the electrodes of Pt/C, RuO_2 and $NiCo_2O_4$ were also characterized. For the electrode preparation, $NiCo_2O_4$@(Ni, Co)OOH sample of 2 mg was dispersed into a 1 mL mixture of water, ethanol and nafion (5 wt. % solution in a mixture of lower aliphatic alcohols and water, Aldrich) with a volume ratio of 1:3.85:0.15, under an ultra-sonication for 30 min. The final catalyst ink suspension has a concentration 2.0 mg·mL^{-1}, and its suspension of 19.8 µL was then transferred onto a polished glassy-carbon electrode of 5 mm in diameter, resulting in a mass loading of 0.2 mg·cm^{-2}.

Measurements of cyclic voltammetry (CV) and linear sweep voltammetry (LSV) were conducted using an electrochemical station (CHI 750D, CH Insruments). Glassy carbon (GC) electrode (5 mm in diameter, Pine Instruments) was used as the working electrode. A graphite electrode was used as the auxiliary electrode, and then Hg/HgO was used as the reference electrode. The electrochemical impedance spectroscope was used (Autolab PGSTAT302N) with a frequency range from 1 mHz to 1 MHz with a potential amplitude of 10 mV. Unless stated otherwise, the tests were made without *i*R compensation in 1.0 M KOH solution.

Measurements using rotating ring-disk electrodes (RRDEs) were conducted in 1 M KOH electrolyte at room temperature using a three-electrode system (Pine Instruments and WaveDriver Workstation). The potentials were measured using the reference data from the Hg/HgO, and a carbon electrode was used as the counter electrode. Several cyclic voltammetry cycles were taken from 0 to 0.8 V (vs Hg/HgO) to stabilize the HER and OER performance of the catalyst before the final polarization curves were recorded. This is because recently it was reported that the amount of Pt deposited onto the catalyst surface after multiple circular scanning improved the catalytic performance.[1] A graphite electrode was used as the counter electrode in this study. All the potentials measured were calibrated with the reversible hydrogen electrode (RHE) using the following equation:

$$E_{RHE} = E_{Hg/HgO} + 0.098V + 0.059\,pH \qquad \text{(S1)}$$

For oxygen evolution reaction OER (or HER) tests, all the electrochemical electrodes were firstly optimized by performing a potential cycling between 1.1 and 1.6 V (or 0 and −0.3V for HER) at 50 mV·s^{-1} in a solution of 1 M KOH until stable voltammogram curves were obtained. Polarization curves and Tafel plots were recorded at two different scan rates of 5 mV·s^{-1} and 0.1 mV·s^{-1}, respectively. Impedance value (R) of the 1M KOH solution was measured to be 6.9 Ω at room temperature. Tafel plots of the samples were obtained according to those reported in the literature. [2, 3] RRDE measurement was conducted in a solution of N_2-saturated 1M KOH for seven times with various rotation speeds (i.e., 400, 620, 900, 1225, 1600, 2025, 2500 r.p.m., respectively).

Elecrochemical Surface Area (ECSA)

The ECSA is the product of R_FS, in which R_F stands for the roughness factors, which is obtained from the ratio of C_{dl} of the test sample and the C_s (= 60 µF cm^{-2}) of a smooth surface;[4] and S stands for the real surface area of the smooth metal electrode, which generally equals to

the geometric area of the carbon electrode.[5] The values of C_{dl} were obtained using acyclic voltammetry and the results are shown in Figures S3a and 3b. The total catalytic activity areas are varied, but in the order from high to low values as follows: $NiCo_2O_4$@(Ni, Co)OOH(296) > RuO_2(91) > Pt/C(6).[6] This suggests that the $NiCo_2O_4$@(Ni, Co)OOH presents a high reaction activity on the same surface area.

Figures S3c and 3d show the results of the rotating ring-disk electrode (RRDE) for HER and OER without *i*R, which are calculated using the KouteckÝ-Levich equation:[7]

$$\frac{1}{i}=\frac{1}{i_K}+\frac{1}{i_L}=\frac{1}{i_K}+\frac{1}{0.62nFAD_O^{2/3}\omega^{1/2}\nu^{-1/6}C_O^*} \qquad (S2)$$

in which *i* is the measured current, i_K and i_L are the kinetic- and diffusion-limiting currents, ω is the angular velocity of the disk (ω=2πN, N is the linear rotation speed), n is the overall number of electrons transferred in oxygen reduction. F is the Faraday constant (F=96 485 $C\cdot mol^{-1}$). A is activity area, C_O is the bulk concentration of O_2, *v* is the kinematic viscosity of the electrolyte, and D_O is the diffusion rate constant. KouteckÝ-Levich plots were obtainedin an N_2-satturated 1M KOH solution using the RRDE and results are shown in Figures S3e and 3f.[3]

The Faradaic efficiency (FE) was obtained according to the previous literature: [8]

$$FE=\frac{I_{ring}}{C_e\times I_{disk}} \qquad (9)$$

Here, I_{disk} is the given current on the disk electrode. I_{ring} is the collection current on the Pt ring electrode at a constant potential of 0.4 V versus RHE. C_e is the oxygen collection coefficient (~0.2) for this type of electrode configuration.

Chronopotentiometry was applied with a given potential (1.53 and -0.3 V) to maintain constant O_2 and H_2 generation. N_2 was constantly purged into the cathodic compartment at a flow rate of 5 $cm^3\cdot min^{-1}$ and the compartment were connected to the gas-sampling loop of a gas chromatograph (GC2020, Hubei Hengxinshiji Scientific Instrument Co.). A thermal conductivity detector (TCD) was used to detect and quantify the generated O_2 and H_2.

Movie S1. The water splitting process of electrolysis cells ($NiCo_2O_4$@(Ni, Co)OOH || $NiCo_2O_4$@(Ni, Co)OOH) recorded at the current density of 100 mA cm^{-2}.

Movie S2. First-principles molecular dynamics (FPMD) simulations animations of movies provides a dynamic model to monitor the water-splitting on the surfaces of $NiCo_2O_4$, (Ni, Co)OOH, and $NiCo_2O_4$@(Ni, Co)OOH, respectively.

Supplementary Figures

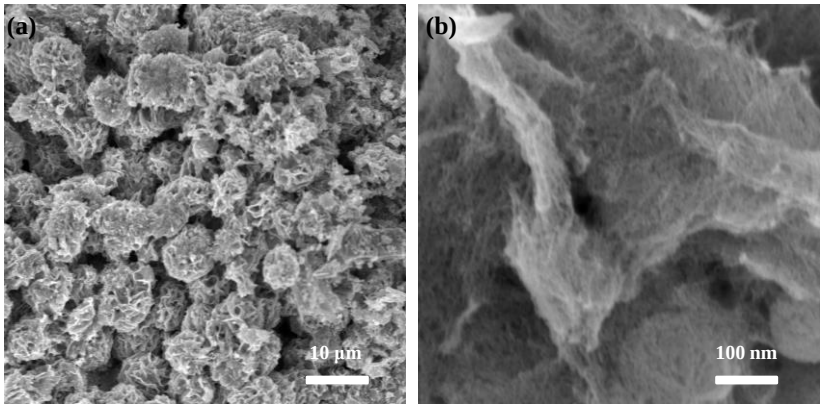

Figure S1. FE-SEM images of coral-like $NiCo_2$-PEG precursor in (a) and (b) the corresponding higher magnifications.

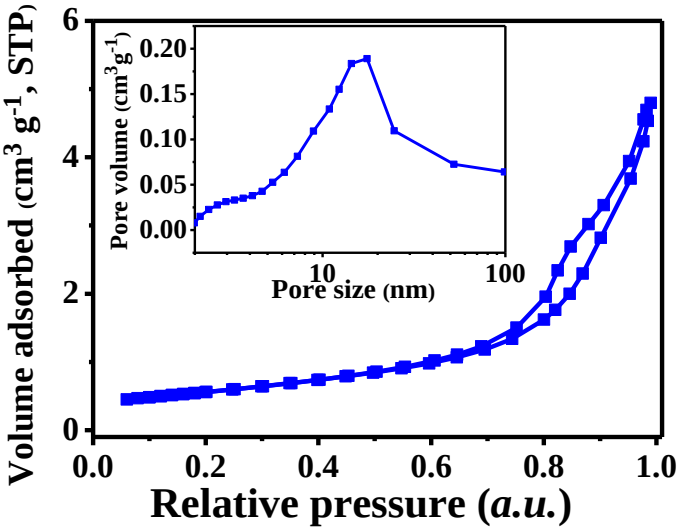

Figure S2. N_2 absorption-desorption isotherm with the pore size distribution (inset).

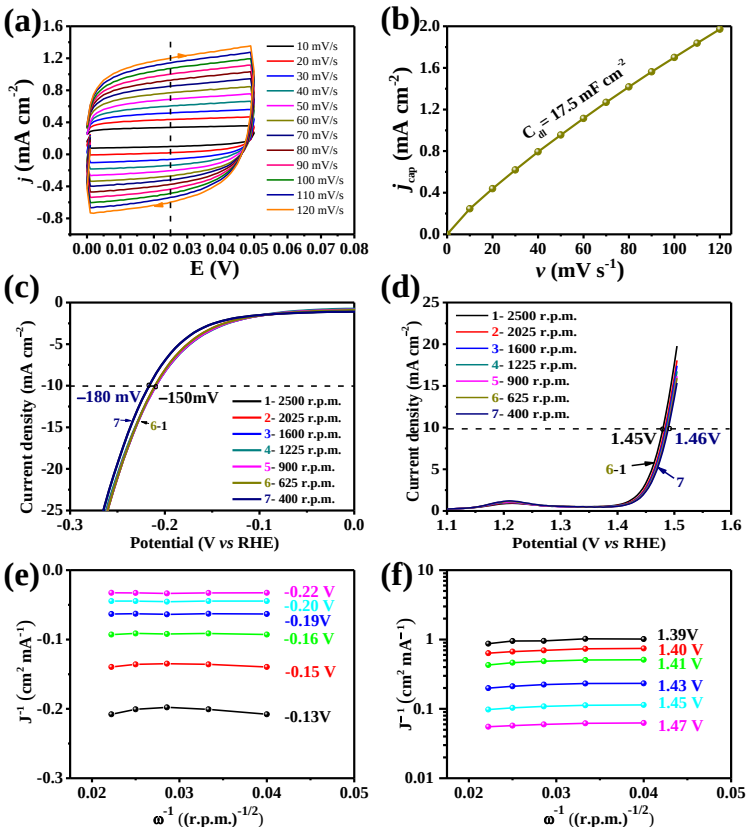

Figure S3. Electrochemical capacitance measurements results; a) typical cyclic voltammograms; b) charging current density differences (*j*) *vs* scan rates curve (*v*) in the potential region 0 − 0.05 V in 1 M KOH at 25 °C; The rotating ring-disk electrode (RRDE) measurements c) HER and d) OER without *i*R with rotation speeds of 400, 625, 900, 1225, 1600, 2025, 2500 r.p.m., respectively; Koutecky-Levich plots of electrocatelyzed e) HER and f) OER for $NiCo_2O_4$@(Ni, Co)OOH

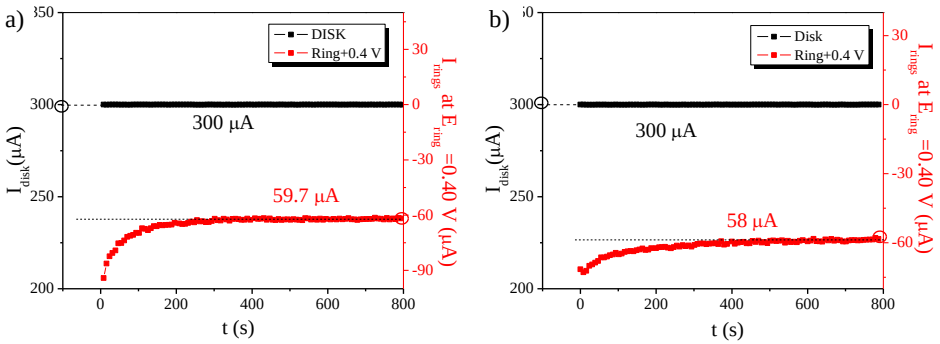

Figure S4. Faraday efficiency of (a) $NiCo_2O_4$@(Ni, Co)OOH and (b) $NiCo_2O_4$ electrodes using the RRDE technique in N_2-saturated 1 M KOH solution. When a constant current (300 μA) was applied to the disk electrode O_2 generation, a ring current was detected immediately.

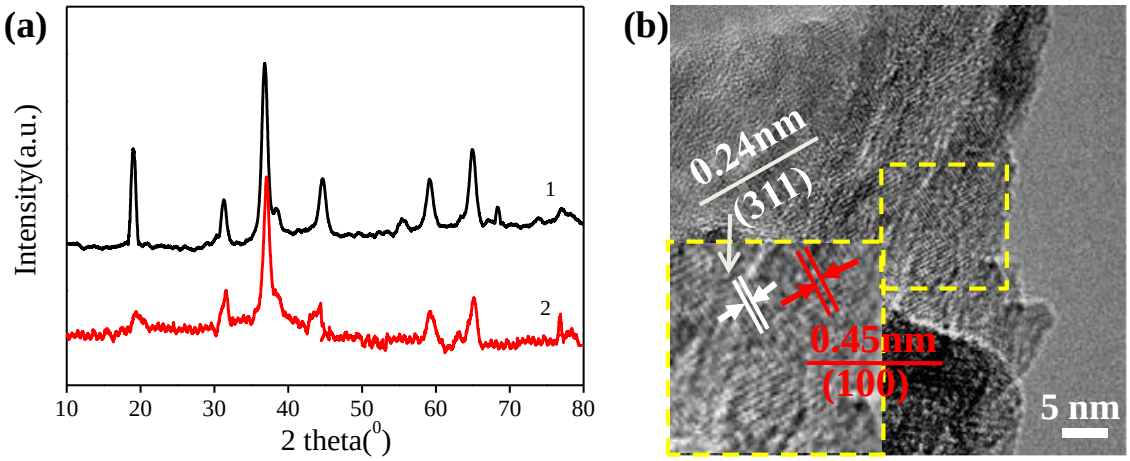

Figure S5. (a) the XRD of $NiCo_2O_4$@(Ni, Co)OOH heterojunction for fresh (curve 1) and 30h sample (curve 2) with the current density increased from 0.1 to 0.6 $A \cdot cm^{-2}$ in the two-electrode device, (b) the HR-TEM after 30h with the current density increased from 0.1 to 0.6 $A \cdot cm^{-2}$ in the two-electrode device

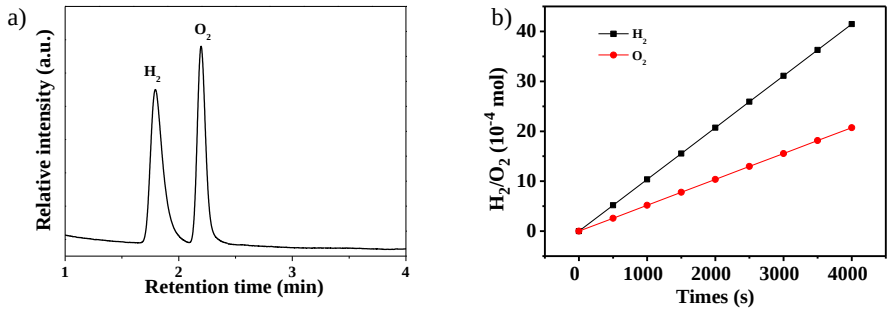

Figure S6. a) Gas chromatography curves of $NiCo_2O_4$@(Ni, Co)OOH after water splitting at the given overpotential of 0.2 V. The gas chromatography survey clearly confirms that the produced bubbles are H_2 and O_2. b) The Faradaic efficiency (FE) of experimental H_2 (red square) and O_2 (red sphere) production versus the theoretic 98% quantities (black solid) for overall water splitting of $NiCo_2O_4$@(Ni, Co)OOH in 1 M KOH at 100 mA·cm^{-2}.

Supplementary Tables

Table S1. Comparison of HER and OER activityfor $NiCo_2O_4$@(Ni, Co)OOH heterojunction with other recently published highly active electrocatalysts in alkaline electrolyte (1 M KOH). Unless stated otherwise, the tests were made in 1.0 M KOH solution.

Catalyst	HER		OER		Reference
	η_{HER} (mV)	Tafel	η_{OER} (mV)	Tafel	
	10 $mA \cdot cm^{-2}$	mV $decade^{-1}$	10 $mA \cdot cm^{-2}$	mV $decade^{-1}$	
$NiCo_2O_4$@(Ni, Co)OOH	120	60	220	48	This work
$NiCo_2O_4$-nanowire	180	63	240	70	*J. Phys. Chem. C*, 2017, **121**, 25888.[6]
$NiCo_2O_4$-nanosheet	290	85	260	53	
$NiCo_2O_4$@NiO@Ni Core/Shell Nanocone Array	120	43	240	58	*Part. Part. Sys. Char.*2017, **34**, 1700228.[9]
$NiCo_2O_4$/NF	164	107	240	51.5	*Adv. Func. Mater.*, 2016, **26**, 3515.[10]
NiFe-LDH/$NiCo_2O_4$/NF	192	59	230	53	*ACS Appl. Mater. Int.* 2017, **9**, 1488.[11]
$NiCo_2O_4$ nanosheet array	105	62.1	270	51.9	*J. Catal.* 2018, **357**, 238.[12]

Table S2. Comparison of overall water-splitting performance for $NiCo_2O_4$@(Ni,Co)OOH heterojunction with the recently reported materials.

Catalyst	Overpotential (mV)			Reference
	10 mA cm^{-2}	20 mA cm^{-2}	100 mA cm^{-2}	
$NiCo_2O_4$@(Ni, Co)OOH	380	430	620	This work
Co1Mn1CH	450	472	770	*J. Am. Chem. Soc.*, 2017, **139**, 8320.[13]
VOOH	390	470	610	*Angew. Chem. Int. Edit.*, 2017, **129**, 588.[14]
RuO_2||Pt-C on CF	240	390	650	*Adv. En. Mater.*, 2017, **7**, 1602579.[15]
Co-doped NiO/$NiFe_2O_4$	353	450	570	*J. Mater. Chem. A*, 2018, **6**, 167.[16]
FeB_2	340	380	-	*Adv. En. Mater.*, 2017, **7**, 1700513.[17]
FeCoNi-LTH/$NiCo_2O_4$/CC	310	400	520	*Acs Appl. Mater. Inter.*, 2017, **9**, 36917.[18]
FeCo-FeCoNi-CC	430	570	-	*ACS Catal.*, 2017, **7**, 469.[19]
Co_3Se_4	360	400	650	*Adv. En. Mater.*, 2017, **7**, 1602579. [15]
CoP-MNA/CoP-MNA	390	430	-	*Adv. Func. Mater.*, 2015, **25**, 7337.[20]
$Ni_{2.5}Co_{0.5}Fe$/NF	390	570	670	*J. Mater. Chem. A*, 2016, **4**, 7245.[21]
$NiCo_2S_4$-NF	400	590	-	*Adv. Func. Mater.*, 2016, **26**, 4661.[22]
$NiCo_2O_4$	420	510	-	*Angew. Chem. Int. Edit.*, 2016, **55**, 6290. [23]
Co_3O_4-MTA	400	470	770	*Angew. Chem. Int. Edit.*, 2017, **56**, 1324. [24]

Supplementary Referencs

1. Y. Luo, D. Huang, M. Li, X. Xiao, W. Shi, M. Wang, J. Su and Y. Shen, *Electrochim. Acta*, 2016, **219**, 187-193.
2. T. Shinagawa, A. T. Garcia-Esparza and K. Takanabe, *Sci. Rep.*, 2015, **5**, 13801.
3. S. Zhao, Y. Wang, J. Dong, C.-T. He, H. Yin, P. An, K. Zhao, X. Zhang, C. Gao, L. Zhang, J. Lv, J. Wang, J. Zhang, A. M. Khattak, N. A. Khan, Z. Wei, J. Zhang, S. Liu, H. Zhao and Z. Tang, *Nature Energy*, 2016, **1**, 16184.
4. S. R. N. Singh J.P., *J. New Mater. Electrochem. Syst.*, 2000, **3**, 137-146.
5. S. Gao, Y. Lin, X. C. Jiao, Y. F. Sun, Q. Q. Luo, W. H. Zhang, D. Q. Li, J. L. Yang and Y. Xie, *Nature*, 2016, **529**, 68-+.
6. L. Tao, Y. Li, M. Li, G. Gao, X. Xiao, M. Wang, X. Jiang, X. Lv, Q. Li, S. Zhang, Z. Zhao, C. Zhao and Y. Shen, *J. Phys. Chem. C*, 2017, **121**, 25888-25897.
7. A. J. Bard and L. R. Faulkner, *J. Chem. Educ.*, 2001, **60**, 80–89.
8. J. Suntivich, K. J. May, H. A. Gasteiger, J. B. Goodenough and Y. Shao-Horn, *Science*, 2011, **334**, 1383-1385.
9. L. Y. Wang, C. D. Gu, X. Ge, J. L. Zhang, H. Y. Zhu and J. P. Tu, *Part. Part. Syst. Char.*, 2017, **34**, 1700228.
10. C. Xiao, Y. Li, X. Lu and C. Zhao, *Adv. Funct. Mater.*, 2016, **26**, 3515-3523.
11. Z. Wang, S. Zeng, W. Liu, X. Wang, Q. Li, Z. Zhao and F. Geng, *ACS Appl. Mat. Interfaces*, 2017, **9**, 1488-1495.
12. L. Fang, Z. Jiang, H. Xu, L. Liu, Y. guan, X. Gu and Y. Wang, *J. Catal.*, 2018, **357**, 238-246.
13. T. Tang, W. J. Jiang, S. Niu, N. Liu, H. Luo, Y. Y. Chen, S. F. Jin, F. Gao, L. J. Wan and J. S. Hu, *J. Am. Chem. Soc.*, 2017, **139**, 8320-8328.
14. H. H. Shi, H. F. Liang, F. W. Ming and Z. C. Wang, *Angew. Chem. Int. Edit.*, 2017, **56**, 573-577.
15. W. Li, X. F. Gao, D. H. Xiong, F. Wei, W. G. Song, J. Y. Xu and L. F. Liu, *Adv. Energy Mater.*, 2017, **7**, 1602579-n/a.
16. Z. Wu, X. Wang, J. Huang and F. Gao, *J. Mater. Chem. A*, 2018, **6**, 167-178.
17. H. Li, P. Wen, Q. Li, C. C. Dun, J. H. Xing, C. Lu, S. Adhikari, L. Jiang, D. L. Carroll and S. M. Geyer, *Adv. Energy Mater.*, 2017, **7**, 1700513-n/a.
18. Y. X. Liu, Y. Bai, Y. Han, Z. Yu, S. M. Zhang, G. H. Wang, J. H. Wei, Q. B. Wu and K. N. Sun, *ACS Appl. Mat. Interfaces*, 2017, **9**, 36917-36926.
19. Y. Yang, Z. Y. Lin, S. Q. Gao, J. W. Su, Z. Y. Lun, G. L. Xia, J. T. Chen, R. R. Zhang and Q. W. Chen, *ACS Catal.*, 2017, **7**, 469-479.
20. Y. P. Zhu, Y. P. Liu, T. Z. Ren and Z. Y. Yuan, *Adv. Funct. Mater.*, 2015, **25**, 7337-7347.
21. X. L. Zhu, C. Tang, H. F. Wang, B. Q. Li, Q. Zhang, C. Y. Li, C. H. Yang and F. Wei, *J. Mater. Chem. A*, 2016, **4**, 7245-7250.
22. A. Sivanantham, P. Ganesan and S. Shanmugam, *Adv. Funct. Mater.*, 2016, **26**, 4661-4672.
23. X. Gao, H. Zhang, Q. Li, X. Yu, Z. Hong, X. Zhang, C. Liang and Z. Lin, *Angew. Chem. Int. Ed.*, 2016, **55**, 6290-6294.
24. Y. P. Zhu, T. Y. Ma, M. Jaroniec and S. Z. Qiao, *Angew. Chem. Int. Edit.*, 2017, **56**, 1324-1328.